

Microwave Quantum Link between Superconducting Circuits Housed in Spatially Separated Cryogenic Systems

P. Magnard^{1,*}, S. Storz¹, P. Kurpiers¹, J. Schär¹, F. Marxer¹, J. Lütolf¹, T. Walter¹, J.-C. Besse¹, M. Gabureac¹, K. Reuer¹, A. Akin¹, B. Royer^{2,‡}, A. Blais^{2,3} and A. Wallraff^{1,4,†}

¹Department of Physics, ETH Zürich, CH-8093 Zürich, Switzerland

²Institut Quantique and Département de Physique, Université de Sherbrooke, Sherbrooke, Québec J1K 2R1, Canada

³Canadian Institute for Advanced Research, Toronto, Ontario M5G 1Z8, Canada

⁴Quantum Center, ETH Zürich, 8093 Zürich, Switzerland



(Received 7 August 2020; accepted 16 November 2020; published 21 December 2020)

Superconducting circuits are a strong contender for realizing quantum computing systems and are also successfully used to study quantum optics and hybrid quantum systems. However, their cryogenic operation temperatures and the current lack of coherence-preserving microwave-to-optical conversion solutions have hindered the realization of superconducting quantum networks spanning different cryogenic systems or larger distances. Here, we report the successful operation of a cryogenic waveguide coherently linking transmon qubits located in two dilution refrigerators separated by a physical distance of five meters. We transfer qubit states and generate entanglement on demand with average transfer and target state fidelities of 85.8% and 79.5%, respectively, between the two nodes of this elementary network. Cryogenic microwave links provide an opportunity to scale up systems for quantum computing and create local area superconducting quantum communication networks over length scales of at least tens of meters.

DOI: 10.1103/PhysRevLett.125.260502

Superconducting circuits are an appealing platform to execute quantum information processing algorithms on noisy-intermediate-scale or error-correctable quantum hardware [1–5] and to study fundamental quantum phenomena [6–9]. Today's state-of-the-art superconducting quantum processors contain a few dozen qubits on a single chip, held at cryogenic temperatures in individual dilution refrigerators. Efforts in qubit integration and packaging [10–13] will likely extend the scale of these processors to thousands of qubits in the foreseeable future. However, limitations such as available wafer size, refrigerated space, and cooling power may arise beyond that scale [14]. Therefore, major innovations in both device integration and cryogenics are required to realize error-corrected quantum computers able to tackle interesting problems intractable on high-performance computing systems, likely requiring millions of qubits [15,16]. Networking quantum processors housed in different cryogenic nodes may provide a modular solution to scale up quantum computers beyond these limitations [17,18]. The capabilities of quantum computers may be extended by forming clusters of networked processors housed in individual cryogenic modules similar to the clusters of processing units used in the high-performance systems.

One approach to realize such networks is to use microwave-to-optical quantum transducers [19–22] with which superconducting circuits may be entangled with optical photons to communicate over long distances in a fashion similar to single atoms [23], trapped ions [24], or defects in diamond [25]. However, despite the constant improvement

of microwave-to-optical transducers, bringing their conversion efficiency, bandwidth, added noise, laser-induced quasiparticle poisoning, and heat loads to practical levels on a single device remains a challenge.

A complementary approach is to connect dilution-refrigerator-based cryogenic systems with cold, superconducting waveguides [26]. This approach could prove advantageous for distributing quantum computing tasks in local cryogenic quantum networks, as it would benefit from readily available, fast, deterministic, error-correctable, and high-fidelity chip-to-chip quantum communication schemes with microwave photons [26–34]. In this Letter, we report the realization of such a cryogenic quantum microwave channel between superconducting qubits located in two distinct dilution refrigerator units. Using a photon shaping technique to transfer excitations deterministically [28,35], we transfer qubit states and generate entanglement on demand between the distant qubits.

Our experimental setup consists of two cryogen-free dilution refrigerators, each of which houses a superconducting circuit with a single qubit cooled to below 20 mK and separated by 5 m (Fig. 1). The two identically designed circuits have a frequency-tunable transmon qubit, each with relaxation and coherence times $T_1 \simeq 12 \mu\text{s}$ and $T_2^e \simeq 6 \mu\text{s}$, coupled dispersively to two Purcell filtered resonators: one for readout and one for excitation transfer, as shown in green and yellow, respectively, in Fig. 1(b). The $|g\rangle$ to $|e\rangle$ transition frequencies of transmon qubits labeled A and B are tuned to $\omega_{q,A}/2\pi = 6.457 \text{ GHz}$ and

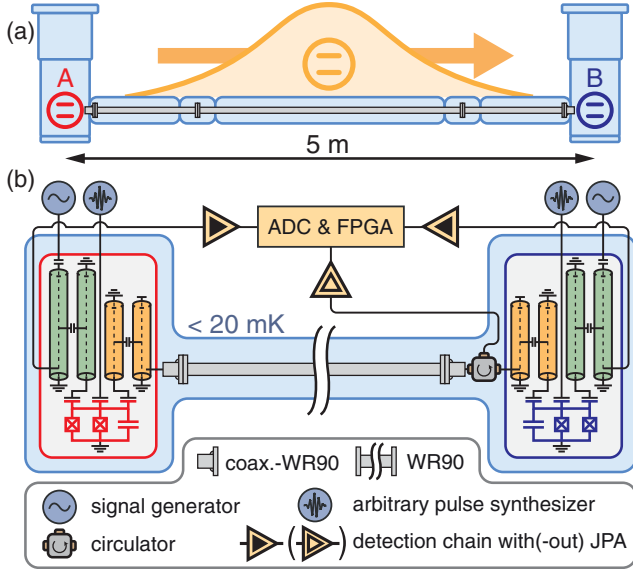


FIG. 1. (a) Schematic representation and (b) simplified circuit diagram of the experimental setup. Each transmon qubit at nodes A (red) and B (blue) is connected to two Purcell filtered $\lambda/4$ resonators: one for readout (green) and one for excitation transfer by emission of a shaped photon (yellow). The light blue background illustrates the refrigerated space.

$\omega_{q,B}/2\pi = 6.074$ GHz, respectively, by applying a magnetic field to their superconducting quantum interference device loops. This adjusts the dispersive shift on each transfer resonator such that their frequencies $\omega_i/2\pi = 8.406$ GHz are matched [28]. Here, $|g\rangle$, $|e\rangle$, and $|f\rangle$ denote the three lowest energy levels of the transmon qubit.

We connect the transfer resonators to each other through a 4.9 m long, superconducting, rectangular aluminum WR90 waveguide in series with two flexible, coaxial copper cables of 0.4 m length each and a circulator. At mK temperatures, the waveguide exhibits attenuation below 1 dB/km over the X band (8–12 GHz), which amounts to a total loss below 10^{-3} over 4.9 m of the waveguide [36]. With attenuation levels comparable to that of optical photons in telecom fibers [44], the waveguide is in principle suited for high-fidelity transmission of microwave photons over intracity scale distances [26].

To perform single-qubit gates, we apply microwave pulses created by arbitrary waveform generators to each qubit through dedicated drive lines. To perform readout, we apply a gated microwave tone to the readout resonator. The transmitted signal is then amplified, down-converted, digitized, and processed by a field-programmable gate array (FPGA). Using quantum-limited Josephson parametric amplifiers (JPA) in the detection chain, we achieve single-shot three-level discrimination of the transmon states with $\sim 5\%$ average error (10% for joint two-qubit readout). Devices, microwave setup, pulse calibration, and qubit readout are discussed in more detail in the Supplemental Material [36].

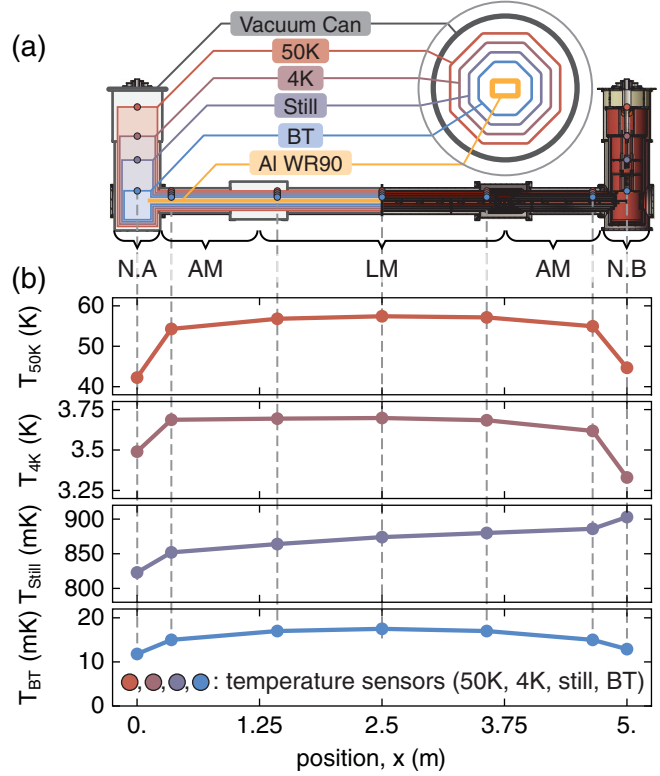


FIG. 2. (a) Longitudinal cross section of a schematic representation (left half) and a 3D model (right half) of the cryogenic system. The inset on the top right shows a transverse cross section of the link. (b) Measured temperature in steady-state vs sensor position x on the axis along the link for all four temperature stages. Nodes A and B: NA and NB; adapter module: AM; link module: LM.

We cool the waveguide to temperatures below 20 mK by mounting it in a custom-made cryogenic system consisting of concentric, octagonal radiation shields held at temperatures of approximately 50 K, 4 K, 850 mK (still), and 15 mK (base temperature) and installed in an o-ring sealed vacuum can [Fig. 2(a)]. See the Supplemental Material for a photograph of the full system [36]. The waveguide is thermalized to the base temperature shield every 0.25 m using flexible copper braids, and the radiation shields are cooled to their equilibrium temperatures using the dilution refrigerators at each end of the system.

The largest heat load on the system is due to room temperature black body radiation, which we mitigate by a set of low-emissivity radiation shields manufactured from high thermal conductivity copper and mechanically supported by thin-walled low thermal conductivity posts. In addition, the heat load on the 50 K stage is reduced by using multilayer insulation [45]. Generally, minimizing the heat flow between shields at different temperature stages and maximizing the thermal conductivity along each stage reduces thermal gradients and thus allows for lower final temperatures. By making the arrangement of shields light-proof, the base temperature shields cool to below 20 mK.

We designed the link to be modular, with 1.25 m long adapter modules to connect the link to each dilution refrigerator and 2.5 m long link modules, which also allow for an extension of the link [Fig. 2(a)]. To compensate for thermal contraction during cooldown, we use flexible copper braids for thermal anchoring between modules. For the same reason, flexible coaxial cables are used to connect the samples to the waveguide.

To monitor the temperature profile of the link, we installed temperature sensors at the positions indicated in Fig. 2(a). Three days after commencing cooldown, the system reaches the steady-state temperature distribution shown in Fig. 2(b), demonstrating the excellent performance of the system. As expected, on each stage, the temperature is lowest at the nodes and the highest in the middle of the link, with an exception for the still stage where we heated node B to 900 mK to optimize cooling power by increasing the flow of ^3He .

To characterize the excitation transfer through the link, we first reset the transmon qubits with microwave drives [46] and apply two consecutive Gaussian π pulses to prepare the qubit and resonator system at node A in the state $|f0\rangle$ [Fig. 3(a)], where $|q\rangle$ and $|n\rangle$ in $|qn\rangle$ denote the transmon state and the transfer resonator Fock state, respectively. We then drive transmon A on the $|f0\rangle \leftrightarrow |g1\rangle$ sideband transition [47,48] to populate the transfer resonator with one photon. This photon couples into the waveguide at rate $\kappa_A/2\pi = 8.9$ MHz and propagates to node B in 28 ns, as estimated from the waveguide length and the relevant group velocities [36]. We shape the $|f0\rangle \leftrightarrow |g1\rangle$ pulse appropriately to emit the photon with a time-symmetric envelope $\phi(t) \propto \text{sech}(\Gamma t/2)$ [28,48,49], where the photon bandwidth Γ can be adjusted up to a maximum value of $\min[\kappa_A, \kappa_B]$. Here we choose $\Gamma/2\pi = \kappa_B/2\pi \simeq 6.2$ MHz to minimize the duration of the protocol. To absorb the photon at node B, we then drive transmon B with an $|f0\rangle \leftrightarrow |g1\rangle$ pulse whose time reverse would emit a photon indistinguishable from the incoming one [35]. Finally, we apply an $e-f$ π pulse on transmon B to map the excitation back to the $g-e$ manifold and then perform a single-shot readout on both qubits. Here and in following experiments, we present data that is corrected for readout errors using reference measurements [36]. For these parameters, the excitation transfer sequence, consisting of the $|f0\rangle \leftrightarrow |g1\rangle$ pulses and the final $e-f$ π pulse, completes in 311 ns.

Truncating the $|f0\rangle \leftrightarrow |g1\rangle$ pulses prematurely at time τ , we characterize the time dependence of the state population of the two transmon qubits throughout the transfer pulse (Fig. 3). As the excitation transfers from node A to node B via the photonic modes (the waveguide and both transfer resonators), the population swaps from the state $|fg\rangle$ of the two spatially separated qubits $|AB\rangle$ to $|ge\rangle$ via the intermediate state $|gg\rangle$. The final two-transmon state populations highlight the different sources of errors in the excitation transfer. The $\sim 3\%$ residual

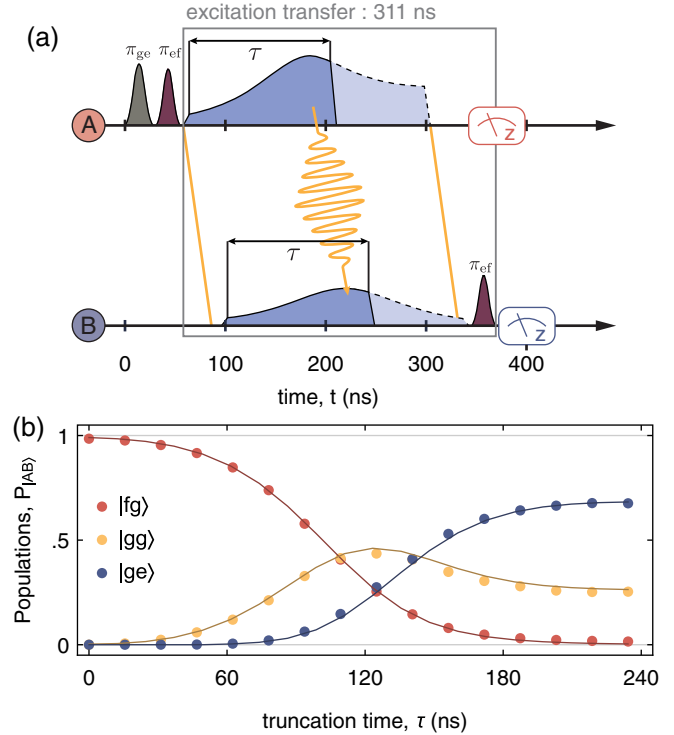


FIG. 3. (a) Pulse scheme used to characterize the excitation transfer dynamics. The $|f0\rangle \rightarrow |g1\rangle$ drives and the $g-e$ and $e-f$ π pulses are represented in blue, gray, and purple, respectively. We use solid and dashed lines for the time-truncated ($\tau = 140$ ns) and full excitation transfer sequences, respectively. The straight yellow lines illustrate the propagation path of the rising and falling edges of the photon in space-time. The subsequence defining the excitation transfer is enclosed in a gray box. (b) Population P in selected two-transmon states $|AB\rangle$ vs $|f0\rangle \leftrightarrow |g1\rangle$ pulse truncation time τ . Solid lines show the results of master equation simulations.

population measured in both $|gf\rangle$ and $|eg\rangle$ (not shown) is due to $e-f$ decay. In case of photon loss or failed absorption during the transfer process, the system ends up in the state $|gg\rangle$. Comparing the measured amplitudes of the fields emitted by A or B using the measurement chain behind the circulator [Fig. 1(b)], we determine a 22.3% photon loss, dominated by the insertion loss of the circulator, and a 4.2% absorption inefficiency [36], which is in reasonable agreement with the 25.3% residual population measured in the state $|gg\rangle$. Finally, the transfer efficiency is characterized by the 67.5% final population in $|ge\rangle$. The time between the applications of the emission and absorption pulses is set to experimentally maximize the transfer efficiency. By comparing the time of arrival of photons emitted from A or B in the photon measurement chain, we determine this optimal time difference to be 38 ns, which decomposes into the photon propagation time and an extra 10 ns lag [36]. Simulations of the transfer dynamics, using the master equation model from Ref. [28] and independently measured parameters, are in

good agreement with the data [solid lines in Fig. 3(b)] and the measured pulse timing [36].

To probe the quantum nature of the excitation transfer, we characterize the qubit state transfer protocol with quantum process tomography. To do so, we reset the qubits to their ground states, prepare A in one of the six mutually unbiased qubit states [50], apply an e - f π pulse on A, and then apply an excitation transfer sequence [Fig. 4(a)]. For each input state $\rho_{i,s}$ we reconstruct the final state $\rho_{f,s}$ of transmon B with three-level quantum state tomography, from which we infer the transfer process matrix χ [36]. We determine an average state fidelity $\mathcal{F}_s = \frac{1}{6} \sum_s \mathcal{F}(\rho_{i,s}, \rho_{f,s}) = 82.4 \pm 0.06\%$ and a process fidelity of $\mathcal{F}_p = \text{Tr}(\chi_{\text{ideal}}\chi) = 75.3 \pm 0.1\%$ relative to the ideal qubit state transfer process. When correcting for readout errors, these fidelities reach $85.8 \pm 0.06\%$ and $79.5 \pm 0.1\%$, respectively [Fig. 4(b)]. On average, the input states have equal populations in $|g\rangle$ and $|e\rangle$, which are transferred in vacuum states, insensitive to loss, with close-to-unit fidelity, and single-photon Fock states, suffering from loss, with a fidelity of 67.5% corresponding to the transfer efficiency. Therefore, the state transfer fidelities \mathcal{F}_s and \mathcal{F}_p can be larger than the photon transfer efficiency if the phase coherence of the process is sufficiently large.

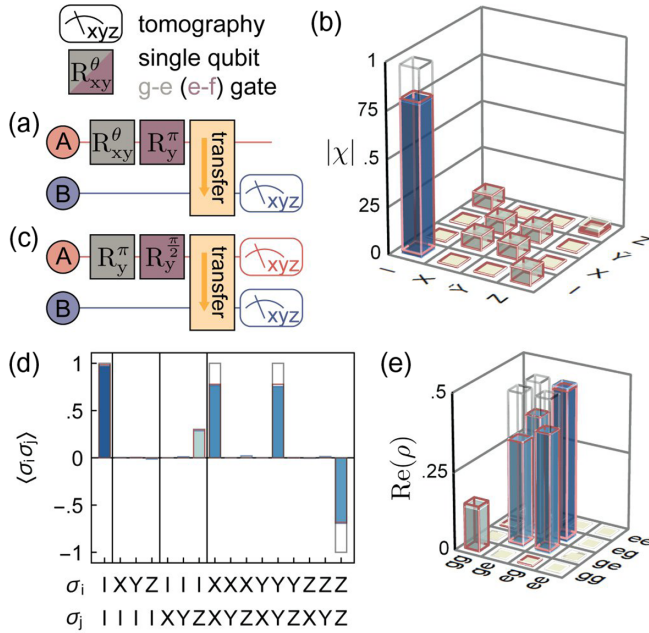


FIG. 4. (a) Quantum circuit used to perform and characterize the qubit state transfer. (b) Absolute value of the qubit state transfer matrix $|\chi|$ in the Pauli basis $\{1, X = \hat{\sigma}_x, Y = i\hat{\sigma}_y, Z = \hat{\sigma}_z\}$. (c) Quantum circuit used to deterministically generate and characterize the Bell state $|\psi^+\rangle$. (d) Expectation value $\langle \sigma_i \sigma_j \rangle$ of the two-qubit Pauli operators, and (e) real part of the density matrix ρ of reconstructed Bell state. In (b),(d),(e), solid blue bars, red wireframes, and gray wireframes are the measured, simulated, and target quantities, respectively.

To generate entanglement across the link, we prepare qubit A in $(|e\rangle + |f\rangle)/\sqrt{2}$, qubit B in $|g\rangle$, and apply the excitation transfer pulses [Fig. 4(c)]. Using quantum state tomography, we reconstruct the two-qubit density matrix $\rho_{3\otimes 3}$ of qubits A and B [36]. To quantify the entanglement with standard metrics, we consider the density matrix ρ , consisting of the two-qubit elements of $\rho_{3\otimes 3}$ [Fig. 4(d),(e)]. We determine the fidelity $\langle \psi^+ | \rho | \psi^+ \rangle = 79.5 \pm 0.1\%$ ($71.9 \pm 0.1\%$) with respect to the ideal Bell state $|\psi^+\rangle = (|ge\rangle + |eg\rangle)/\sqrt{2}$, and evaluate a concurrence of $C(\rho) = 0.746 \pm 0.003$ (0.588 ± 0.002), with (without) correction for readout errors.

Simulations of the qubit state transfer and entanglement generation sequences are in good agreement with the measurement results, as quantified by the small trace distances $\sqrt{\text{Tr}(|\chi - \chi_{\text{sim}}|^2)} = 0.09$ and $\sqrt{\text{Tr}(|\rho - \rho_{\text{sim}}|^2)} = 0.023$ between the reconstructed and simulated quantities. These simulations suggest that photon loss and transmon decay are the dominant sources of errors in these protocols, contributing to 11.8% and $\sim 6\%$ infidelity, respectively. In future experiments, the photon loss may be reduced to 5% by removing the circulator [31–34], by using a printed circuit board metalized with a superconductor, and by using low-loss coaxial cables between the device and the waveguide. Simulations of the protocols with 5% photon loss and reasonably improved coherence times ($T_1 \simeq T_2^e \simeq 30 \mu\text{s}$) and transfer resonator bandwidth ($\kappa/2\pi = 12 \text{ MHz}$) indicate that Bell state fidelities and state transfer process fidelities as high as 96% may be achievable, which may enable distributed surface-code computation [17] and communication [51] between distant cryogenic nodes. Further improvement may be obtainable using protocols requiring less time compared to the coherence of the circuit elements [31] or ones that are resilient to photon loss [33,34,52,53] and thermal excitation [26,27].

This realization of a meter-scale, mK temperature, microwave-frequency coherent quantum link and its use for quantum state transfer and entanglement generation suggests a number of directions for future research. For example, we plan to experimentally investigate the distribution of quantum information processing tasks between quantum nodes hosting multiple qubits using a coherent cryogenic network, an essential part of a modular quantum computer architecture [54]. In addition, the modularity of the cryogenic link demonstrated here offers a straightforward path toward extending the physical distance between nodes by adding modules to the link. Due to the small photon loss in the superconducting rectangular waveguide, cryogenic links covering distances of tens or even hundreds of meters could be realized, primarily limited by financial constraints imposed by the thermal requirements. On such length scales, one may investigate nonlocal physics [55,56] or non-Markovian waveguide QED [57,58] with superconducting quantum devices and set the grounds for microwave quantum local area networks [26].

This work is supported by the European Research Council (ERC) through the ‘‘Superconducting Quantum Networks’’ (SuperQuNet) project, by the National Centre of Competence in Research ‘‘Quantum Science and Technology’’ (NCCR QSIT), a research instrument of the Swiss National Science Foundation (SNSF), by ETH Zurich, by NSERC, the Canada First Research Excellence Fund, and by the Vanier Canada Graduate Scholarships. P. M., S. S., P. K. and T. W. designed and developed the experiment. J.-C. B., T. W. and M. G. fabricated the samples. J. L., P. K., P. M., S. S., F. M., and J. S. designed, characterized, and assembled the cryogenic system. P. M., P. K., and S. S. performed the experiments. P. M., P. K., and A. W. analyzed and interpreted the data. P. M., K. R., A. A., J. S., and F. M. implemented the FPGA firmware and experiment automation. B. R., P. M., and P. K. performed the master equation simulations. P. M. and A. W. wrote the manuscript. All authors commented on the manuscript. The project was led by A. W.

*Corresponding author.

paul.magnard@phys.ethz.ch

†Corresponding author.

andreas.wallraff@phys.ethz.ch

*Present Address: Department of Physics, Yale University, New Haven, Connecticut 06520, USA.

- [1] J. Preskill, Quantum computing in the NISQ era and beyond, *Quantum* **2**, 79 (2018).
- [2] F. Arute *et al.*, Quantum supremacy using a programmable superconducting processor, *Nature (London)* **574**, 505 (2019).
- [3] A. Kandala, K. Temme, A. D. Córcoles, A. Mezzacapo, J. M. Chow, and J. M. Gambetta, Error mitigation extends the computational reach of a noisy quantum processor, *Nature (London)* **567**, 491 (2019).
- [4] N. Ofek, A. Petrenko, R. Heeres, P. Reinhold, Z. Leghtas, B. Vlastakis, Y. Liu, L. Frunzio, S. M. Girvin, L. Jiang, M. Mirrahimi, M. H. Devoret, and R. J. Schoelkopf, Extending the lifetime of a quantum bit with error correction in superconducting circuits, *Nature (London)* **536**, 441 (2016).
- [5] C. K. Andersen, A. Remm, S. Lazar, S. Krinner, N. Lacroix, G. J. Norris, M. Gabureac, C. Eichler, and A. Wallraff, Repeated quantum error detection in a surface code, *Nat. Phys.* **16**, 875 (2020).
- [6] A. van Loo, A. Fedorov, K. Lalumière, B. Sanders, A. Blais, and A. Wallraff, Photon-mediated interactions between distant artificial atoms, *Science* **342**, 1494 (2013).
- [7] S. Hacoen-Gourgy, L. S. Martin, E. Flurin, V. V. Ramasesh, K. B. Whaley, and I. Siddiqi, Quantum dynamics of simultaneously measured non-commuting observables, *Nature (London)* **538**, 491 (2016).
- [8] N. Cottet, S. Jezouin, L. Bretheau, P. Campagne-Ibarcq, Q. Ficheux, J. Anders, A. Auffèves, R. Azouit, P. Rouchon, and B. Huard, Observing a quantum Maxwell demon at work, *Proc. Natl. Acad. Sci. U.S.A.* **114**, 7561 (2017).
- [9] Z. K. Mineev, S. O. Mundhada, S. Shankar, P. Reinhold, R. Gutiérrez-Jáuregui, R. J. Schoelkopf, M. Mirrahimi, H. J. Carmichael, and M. H. Devoret, To catch and reverse a quantum jump mid-flight, *Nature (London)* **570**, 200 (2019).
- [10] J. H. Béjanin, T. G. McConkey, J. R. Rinehart, C. T. Earnest, C. R. H. McRae, D. Shiri, J. D. Bateman, Y. Rohanizadegan, B. Penava, P. Breul, S. Royak, M. Zapatka, A. G. Fowler, and M. Mariantoni, Three-Dimensional Wiring for Extensible Quantum Computing: The Quantum Socket, *Phys. Rev. Applied* **6**, 044010 (2016).
- [11] R. N. Das, J. L. Yoder, D. Rosenberg, D. K. Kim, D. Yost, J. Mallek, D. Hover, V. Bolkhovskiy, A. J. Kerman, and W. D. Oliver, Cryogenic qubit integration for quantum computing, in *IEEE 68th Electronic Components and Technology Conference (ECTC)* (IEEE, San Diego, CA, 2018), <https://dx.doi.org/10.1109/ECTC.2018.00080>.
- [12] B. Foxen *et al.*, Qubit compatible superconducting interconnects, *Quantum Sci. Technol.* **3**, 014005 (2018).
- [13] C. U. Lei, L. Krayzman, S. Ganjam, L. Frunzio, and R. J. Schoelkopf, High coherence superconducting microwave cavities with indium bump bonding, *Appl. Phys. Lett.* **116**, 154002 (2020).
- [14] S. Krinner, S. Storz, P. Kurpiers, P. Magnard, J. Heinsoo, R. Keller, J. Lütolf, C. Eichler, and A. Wallraff, Engineering cryogenic setups for 100-qubit scale superconducting circuit systems, *Eur. Phys. J. Quantum Technol.* **6**, 2 (2019).
- [15] M. Reiher, N. Wiebe, K. M. Svore, D. Wecker, and M. Troyer, Elucidating reaction mechanisms on quantum computers, *Proc. Natl. Acad. Sci. U.S.A.* **114**, 7555 (2017).
- [16] R. Babbush, C. Gidney, D. W. Berry, N. Wiebe, J. McClean, A. Paler, A. Fowler, and H. Neven, Encoding Electronic Spectra in Quantum Circuits with Linear T Complexity, *Phys. Rev. X* **8**, 041015 (2018).
- [17] N. H. Nickerson, J. F. Fitzsimons, and S. C. Benjamin, Freely Scalable Quantum Technologies Using Cells of 5-to-50 Qubits with Very Lossy and Noisy Photonic Links, *Phys. Rev. X* **4**, 041041 (2014).
- [18] T. Brecht, W. Pfaff, C. Wang, Y. Chu, L. Frunzio, M. H. Devoret, and R. J. Schoelkopf, Multilayer microwave integrated quantum circuits for scalable quantum computing, *npj Quantum Inf.* **2**, 16002 (2016).
- [19] L. Fan, C.-L. Zou, R. Cheng, X. Guo, X. Han, Z. Gong, S. Wang, and H. X. Tang, Superconducting cavity electro-optics: A platform for coherent photon conversion between superconducting and photonic circuits, *Sci. Adv.* **4**, eaar4994 (2018).
- [20] A. P. Higginbotham, P. S. Burns, M. D. Urmey, R. W. Peterson, N. S. Kampel, B. M. Brubaker, G. Smith, K. W. Lehnert, and C. A. Regal, Harnessing electro-optic correlations in an efficient mechanical converter, *Nat. Phys.* **14**, 1038 (2018).
- [21] M. Forsch, R. Stockill, A. Wallucks, I. Marinković, C. Gärtner, R. A. Norte, F. van Otten, A. Fiore, K. Srinivasan, and S. Gröblacher, Microwave-to-optics conversion using a mechanical oscillator in its quantum ground state, *Nat. Phys.* **16**, 69 (2020).
- [22] M. Mirhosseini, A. Sipahigil, M. Kalaei, and O. Painter, Quantum transduction of optical photons from a superconducting qubit, [arXiv:2004.04838](https://arxiv.org/abs/2004.04838).
- [23] J. Hofmann, M. Krug, N. Ortegel, L. Gérard, M. Weber, W. Rosenfeld, and H. Weinfurter, Heralded entanglement

- between widely separated atoms, *Science* **337**, 72 (2012).
- [24] D. L. Moehring, P. Maunz, S. Olmschenk, K. C. Younge, D. N. Matsukevich, L. M. Duan, and C. Monroe, Entanglement of single-atom quantum bits at a distance, *Nature (London)* **449**, 68 (2007).
- [25] H. Bernien, B. Hensen, W. Pfaff, G. Koolstra, M. S. Blok, L. Robledo, T. H. Taminau, M. Markham, D. J. Twitchen, L. Childress, and R. Hanson, Heralded entanglement between solid-state qubits separated by three metres, *Nature (London)* **497**, 86 (2013).
- [26] Z.-L. Xiang, M. Zhang, L. Jiang, and P. Rabl, Intracavity Quantum Communication via Thermal Microwave Networks, *Phys. Rev. X* **7**, 011035 (2017).
- [27] B. Vermersch, P.-O. Guimond, H. Pichler, and P. Zoller, Quantum State Transfer via Noisy Photonic and Phononic Waveguides, *Phys. Rev. Lett.* **118**, 133601 (2017).
- [28] P. Kurpiers, P. Magnard, T. Walter, B. Royer, M. Pechal, J. Heinsoo, Y. Salathé, A. Akin, S. Storz, J.-C. Besse, S. Gasparinetti, A. Blais, and A. Wallraff, Deterministic quantum state transfer and remote entanglement using microwave photons, *Nature (London)* **558**, 264 (2018).
- [29] P. Campagne-Ibarcq, E. Zaly-Geller, A. Narla, S. Shankar, P. Reinhold, L. Burkhardt, C. Axline, W. Pfaff, L. Frunzio, R. J. Schoelkopf, and M. H. Devoret, Deterministic Remote Entanglement of Superconducting Circuits Through Microwave Two-Photon Transitions, *Phys. Rev. Lett.* **120**, 200501 (2018).
- [30] C. Axline, L. Burkhardt, W. Pfaff, M. Zhang, K. Chou, P. Campagne-Ibarcq, P. Reinhold, L. Frunzio, S. M. Girvin, L. Jiang, M. H. Devoret, and R. J. Schoelkopf, On-demand quantum state transfer and entanglement between remote microwave cavity memories, *Nat. Phys.* **14**, 705 (2018).
- [31] Y. P. Zhong, H.-S. Chang, K. J. Satzinger, M.-H. Chou, A. Bienfait, C. R. Conner, É. Dumur, J. Grebel, G. A. Peairs, R. G. Povey, D. I. Schuster, and A. N. Cleland, Violating Bell's inequality with remotely connected superconducting qubits, *Nat. Phys.* **15**, 741 (2019).
- [32] N. Leung, Y. Lu, S. Chakram, R. K. Naik, N. Earnest, R. Ma, K. Jacobs, A. N. Cleland, and D. I. Schuster, Deterministic bidirectional communication and remote entanglement generation between superconducting qubits, *npj Quantum Inf.* **5**, 18 (2019).
- [33] H.-S. Chang, Y. P. Zhong, A. Bienfait, M.-H. Chou, C. R. Conner, E. Dumur, J. Grebel, G. A. Peairs, R. G. Povey, K. J. Satzinger, and A. N. Cleland, Remote Entanglement via Adiabatic Passage Using a Tunably Dissipative Quantum Communication System, *Phys. Rev. Lett.* **124**, 240502 (2020).
- [34] L. D. Burkhardt, J. Teoh, Y. Zhang, C. J. Axline, L. Frunzio, M. H. Devoret, L. Jiang, S. M. Girvin, and R. J. Schoelkopf, Error-detected state transfer and entanglement in a superconducting quantum network, [arXiv:2004.06168](https://arxiv.org/abs/2004.06168).
- [35] J. I. Cirac, P. Zoller, H. J. Kimble, and H. Mabuchi, Quantum State Transfer and Entanglement Distribution Among Distant Nodes in a Quantum Network, *Phys. Rev. Lett.* **78**, 3221 (1997).
- [36] See Supplemental Material, which includes Refs. [37–43], at <http://link.aps.org/supplemental/10.1103/PhysRevLett.125.260502> for details about the characterization of waveguide loss, for details about the sample fabrication and parameters, for a complete wiring diagram of the setup, for details about the calibration of pulses and their relative timings, for details about qutrit single-shot readout, for a photograph of the full cryogenic system, for details about the characterization of some properties of the transfer via measurement of photon envelopes, and for details about the tomographic reconstruction methods.
- [37] P. Kurpiers, T. Walter, P. Magnard, Y. Salathe, and A. Wallraff, Characterizing the attenuation of coaxial and rectangular microwave-frequency waveguides at cryogenic temperatures, *Eur. Phys. J. Quantum Technol.* **4**, 8 (2017).
- [38] D. M. Pozar, *Microwave Engineering*, 4th ed. (Wiley & Sons, Inc., New Jersey, USA, 2012).
- [39] T. Walter, P. Kurpiers, S. Gasparinetti, P. Magnard, A. Potočnik, Y. Salathé, M. Pechal, M. Mondal, M. Oppliger, C. Eichler, and A. Wallraff, Rapid, High-Delity, Single-Shot Dispersive Readout of Superconducting Qubits, *Phys. Rev. Applied* **7**, 054020 (2017).
- [40] K. Geerlings, Z. Leghtas, I. M. Pop, S. Shankar, L. Frunzio, R. J. Schoelkopf, M. Mirrahimi, and M. H. Devoret, Demonstrating a Driven Reset Protocol for a Superconducting Qubit, *Phys. Rev. Lett.* **110**, 120501 (2013).
- [41] K. Serniak, M. Hays, G. de Lange, S. Diamond, S. Shankar, L. D. Burkhardt, L. Frunzio, M. Houzet, and M. H. Devoret, Hot Nonequilibrium Quasiparticles in Transmon Qubits, *Phys. Rev. Lett.* **121**, 157701 (2018).
- [42] F. Motzoi, J. M. Gambetta, P. Rebentrost, and F. K. Wilhelm, Simple Pulses for Elimination of Leakage in Weakly Nonlinear Qubits, *Phys. Rev. Lett.* **103**, 110501 (2009).
- [43] I. L. Chuang and M. A. Nielsen, Prescription for experimental determination of the dynamics of a quantum black box, *J. Mod. Opt.* **44**, 2455 (1997).
- [44] Y. Tamura, H. Sakuma, K. Morita, M. Suzuki, Y. Yamamoto, K. Shimada, Y. Honma, K. Sohma, T. Fujii, and T. Hasegawa, The first 0.14-dB/km loss optical fiber and its impact on submarine transmission, *J. Light. Technol.* **36**, 44 (2018).
- [45] V. Parma, Cryostat Design, CAS—CERN Accelerator School: Course on Superconductivity for Accelerators, <https://doi.org/10.5170/CERN-2014-005.353> (2014).
- [46] P. Magnard, P. Kurpiers, B. Royer, T. Walter, J.-C. Besse, S. Gasparinetti, M. Pechal, J. Heinsoo, S. Storz, A. Blais, and A. Wallraff, Fast and Unconditional All-Microwave Reset of a Superconducting Qubit, *Phys. Rev. Lett.* **121**, 060502 (2018).
- [47] S. Zeytinoğlu, M. Pechal, S. Berger, A. A. Abdumalikov Jr., A. Wallraff, and S. Filipp, Microwave-induced amplitude- and phase-tunable qubit-resonator coupling in circuit quantum electrodynamics, *Phys. Rev. A* **91**, 043846 (2015).
- [48] M. Pechal, L. Huthmacher, C. Eichler, S. Zeytinoğlu, A. A. Abdumalikov Jr., S. Berger, A. Wallraff, and S. Filipp, Microwave-Controlled Generation of Shaped Single Photons in Circuit Quantum Electrodynamics, *Phys. Rev. X* **4**, 041010 (2014).
- [49] O. Morin, M. Körber, S. Langenfeld, and G. Remppe, Deterministic Shaping and Reshaping of Single-Photon Temporal Wave Functions, *Phys. Rev. Lett.* **123**, 133602 (2019).

- [50] S. J. van Enk, N. Lütkenhaus, and H. J. Kimble, Experimental procedures for entanglement verification, *Phys. Rev. A* **75**, 052318 (2007).
- [51] A. G. Fowler, D. S. Wang, C. D. Hill, T. D. Ladd, R. Van Meter, and L. C. L. Hollenberg, Surface Code Quantum Communication, *Phys. Rev. Lett.* **104**, 180503 (2010).
- [52] P. Kurpiers, M. Pechal, B. Royer, P. Magnard, T. Walter, J. Heinsoo, Y. Salathé, A. Akin, S. Storz, J.-C. Besse, S. Gasparinetti, A. Blais, and A. Wallraff, Quantum Communication with Time-Bin Encoded Microwave Photons, *Phys. Rev. Applied* **12**, 044067 (2019).
- [53] K. Bergmann *et al.*, Roadmap on STIRAP applications, *J. Phys. B* **52**, 202001 (2019).
- [54] J. I. Cirac, A. K. Ekert, S. F. Huelga, and C. Macchiavello, Distributed quantum computation over noisy channels, *Phys. Rev. A* **59**, 4249 (1999).
- [55] B. Hensen, H. Bernien, A. E. Dreau, A. Reiserer, N. Kalb, M. S. Blok, J. Ruitenberg, R. F. L. Vermeulen, R. N. Schouten, C. Abellan, W. Amaya, V. Pruneri, M. W. Mitchell, M. Markham, D. J. Twitchen, D. Elkouss, S. Wehner, T. H. Taminiau, and R. Hanson, Loophole-free Bell inequality violation using electron spins separated by 1.3 kilometres, *Nature (London)* **526**, 682 (2015).
- [56] P. Bierhorst, E. Knill, S. Glancy, Y. Zhang, A. Mink, S. Jordan, A. Rommal, Y.-K. Liu, B. Christensen, S. W. Nam, M. J. Stevens, and L. K. Shalm, Experimentally generated randomness certified by the impossibility of superluminal signals, *Nature (London)* **556**, 223 (2018).
- [57] F. Dinc and A. M. Branczyk, Non-markovian super-superradiance in a linear chain of up to 100 qubits, *Phys. Rev. Research* **1**, 032042 (2019).
- [58] G. Calajó, Y.-L. L. Fang, H. U. Baranger, and F. Ciccarello, Exciting a bound state in the continuum through multiphoton scattering plus delayed quantum feedback, *Phys. Rev. Lett.* **122**, 073601 (2019).

Microwave Quantum Link between Superconducting Circuits Housed in Spatially Separated Cryogenic Systems Supplemental Material

S1. MEASUREMENT OF WAVEGUIDE LOSS

To estimate the loss in the rectangular waveguide connecting nodes A and B, we measure the attenuation constant of a similar waveguide using the resonant cavity technique described in Ref. [S1]. The device under test consists of two pieces of rectangular waveguide of the WR90 type, made of AL6061 aluminum without any surface treatment. The two pieces, of 12" (304.8 mm) and 2.5 m, respectively, are joined in a flange-to-flange flat connection and held below 15 mK inside a dedicated cryogenic system made of a cryogenic node and a 3.75 m long cryogenic arm (Fig. S1 a). Both ends of the waveguide are closed with aluminum plates with an aperture hole, to form a multi-mode 3D cavity displaying an inter-mode frequency spacing ranging from 30 MHz to 45 MHz through the X band. The dimensions of the aperture holes are chosen such that the cavity modes are under-coupled.

Using a vector network analyzer (VNA), we measure selected resonance peaks between 7.5 GHz and 11 GHz in transmission, and fit them to a Lorentzian curve to extract their loaded quality factor Q (Fig. S1 b and c). The loaded quality factor being a lower bound to the internal quality factor Q_i , we determine an upper-bound to the attenuation constant [S1, S2]

$$\alpha(\nu) = \frac{1}{Q(\nu)} \frac{2\pi\nu}{c\sqrt{1 - \left(\frac{c}{2a\nu}\right)^2}}, \quad (\text{S1})$$

where ν is the resonance frequency, c is the speed of light in vacuum and $a = 22.86$ mm is the width of the waveguide. The attenuation constant is found to be below 1 dB/km for all measured data points (Fig. S1 d).

S2. CHIP FABRICATION, DEVICE PARAMETERS AND MEASUREMENT SETUP

We fabricated the two samples on $4.3 \text{ mm} \times 7 \text{ mm}$ silicon substrates. We patterned the qubit pad and the coplanar waveguide (CPW) structures in a 150 nm thick niobium film sputtered on a silicon substrate with reactive ion etching in a photolithographic process. In a second photolithographic step, we deposited Al/Ti/Al airbridges to connect the ground plane at selected places across the CPWs. We fabricated the Al/AlO_x/Al Josephson junctions in a third step with electron-beam lithography and double-angle shadow evaporation. Each sample (Fig. S2) was then mounted, glued and wire-bonded to a copper PCB, which was packaged in a copper sample holder. We mounted each sample holder to the

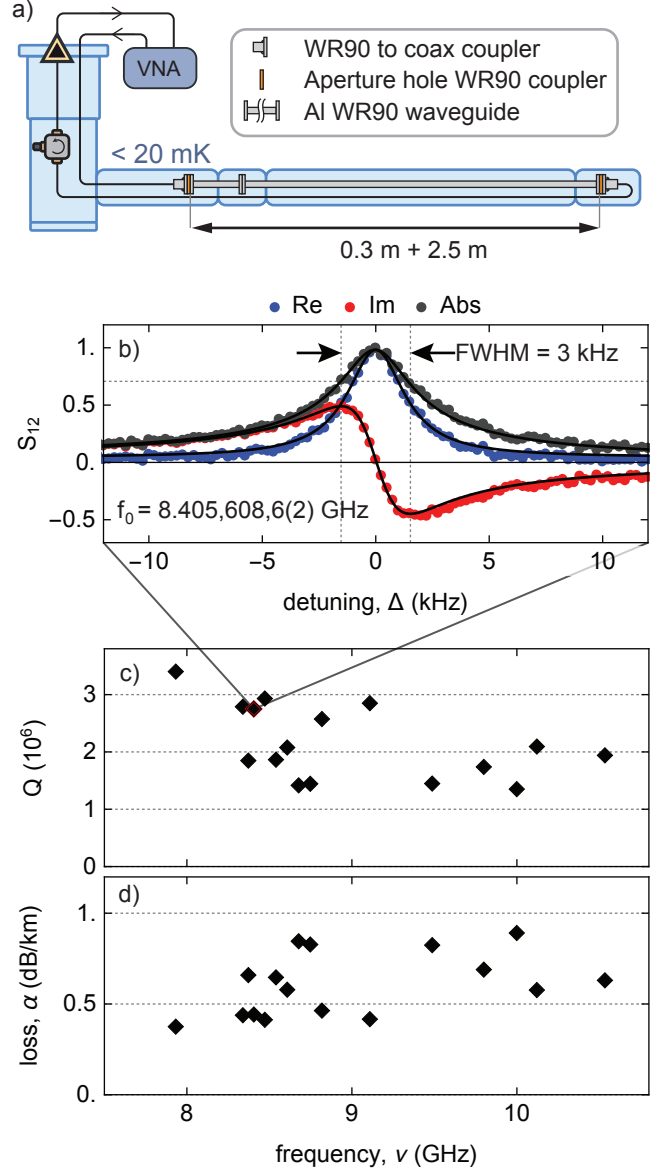


FIG. S1. a) Schematic diagram of the waveguide loss characterization experiment, using the same legend as in Fig. 1 of the main text. b) Real part (blue), imaginary part (red) and absolute value (black) of the transmission spectrum S_{12} around a waveguide cavity mode resonance at $f_0 = 8.405,608,6(2)$ GHz. c) Loaded quality factor Q , and d), loss rate α vs resonance frequency ν for selected waveguide cavity mode resonances.

base plate of the corresponding dilution refrigerator and wired the devices to the instruments as documented in the wiring diagram Fig. S4. Note that the cryogenic sys-

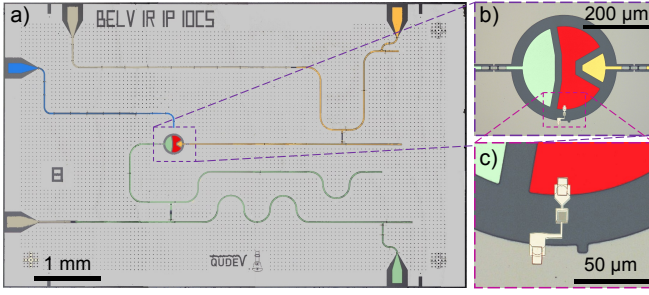


FIG. S2. a) False color photograph of a chip similar to those used in the experiment, before deposition of the Josephson junctions, showing the transmon island (red), the drive line (blue), the readout circuitry (green) and the transfer circuitry (yellow). b) Microscope image of the transmon qubit, after deposition of the Josephson junctions. c) Enlarged view of the Josephson junctions, see scale bars.

tem is connected only via one transmission line to the ground of the instrument setup. All other lines have inner/outer DC-blocks to avoid ground loops, which could introduce detrimental noise to the setup.

For each chip, we characterized the parameters of the readout and transfer resonator and Purcell filter circuitry, including resonant frequencies, coupling rates and dispersive shifts, from the transmission spectra through their respective Purcell filtering resonator with the transmon initialized in state $|g\rangle$ or $|e\rangle$, using methods and models similar to those described in Ref. [S3]. Using Ramsey-type experiments, we extracted the transition frequencies and coherence times of the three-level transmon qubits. Both chips have similar parameters (Table SI). However, because we tuned qubit A and B to different operating frequencies, qubit frequency dependent parameters such as the qubit/resonator shifts and the $|f0\rangle \leftrightarrow |g1\rangle$ transition frequencies are different at node A and B. The transfer Purcell filter bandwidth differs significantly between the samples, which we suspect to be due to the sensitivity of this parameter to the output impedance.

Using the procedure described in Ref. [S4], we measured a transmon thermal population at equilibrium of approximately 16% for each qubit. We suspect that the absence of infra-red filters in the cables connecting to the samples, and of radiation tight base temperature shields at the node cryostats, leading to poor infra-red shielding, causes this high effective transmon temperature [S5], which we chose to mitigate in future experiments.

To perform our protocol with high fidelity despite a significant initial thermal population, we reset both transmon qubits at the beginning of each experiment cycle using the method presented in Ref. [S6]. We simultaneously drive the e - f and $|f0\rangle \leftrightarrow |g1\rangle$ transitions with two resonant, flat-top pulses to couple the states $|e0\rangle$ and $|f0\rangle$ to state $|g1\rangle$, which decays to $|g0\rangle$ at a high rate κ into a cold, $50\ \Omega$ environment (the photon detection line in this case). Calibrating the drive rates as described in [S6], this leads to an unconditional qutrit reset at rate $\kappa/3$.

quantity, symbol	unit	Node A	Node B
qubit transition frequency, $\omega_q/2\pi$	GHz	6.457	6.074
transmon anharmonicity, $\alpha/2\pi$	MHz	-262	-262
energy relaxation time on ge , T_{1ge}	μs	12.2	11.7
energy relaxation time on ef , T_{1ef}	μs	4.9	5.0
coherence time on ge , T_{2ge}^e	μs	7.6	5.0
coherence time on ef , T_{2ef}^e	μs	7.1	5.0
thermal excitation at equilibrium, n_{th}	%	16.2	16.8
$ f, 0\rangle \leftrightarrow g, 1\rangle$ transition frequency, ν_{f0g1}	GHz	4.022	3.485
readout resonator frequency, $\omega_r/2\pi$	GHz	4.698	4.701
readout Purcell filter frequency, $\omega_{Pr}/2\pi$	GHz	4.704	4.723
readout resonator/qubit coupling, $g_r/2\pi$	MHz	202	214
readout circuit dispersive shift, $\chi_r/2\pi$	MHz	-4.1	-7.9
readout resonator/filter coupling, $J_r/2\pi$	MHz	19.9	20.0
readout Purcell filter bandwidth, $\kappa_{Pr}/2\pi$	MHz	71	67
readout resonator eff. bandwidth, $\kappa_r/2\pi$	MHz	21.7	16.8
transfer resonator frequency, $\omega_t/2\pi$	GHz	8.406	8.406
transfer Purcell filter frequency, $\omega_{Pt}/2\pi$	GHz	8.444	8.470
transfer resonator/qubit coupling, $g_t/2\pi$	MHz	307	306
transfer circuit dispersive shift, $\chi_t/2\pi$	MHz	-5.75	-4.0
transfer resonator/filter coupling, $J_t/2\pi$	MHz	20	20.8
transfer Purcell filter bandwidth, $\kappa_{Pt}/2\pi$	MHz	110	155
transfer resonator eff. bandwidth, $\kappa_t/2\pi$	MHz	8.6	6.25

TABLE SI. Device parameters for chips A and B.

We set the duration of the reset pulses to $1\ \mu\text{s}$, exceeding the characteristic reset time $3/\kappa$ by more than a factor of 10, to minimize residual qubit excitation. We did not determine the residual excitation left after active reset explicitly. However, assuming that the reset is limited by spontaneous rethermalization, we estimate a residual excitation after reset of 0.08% (0.12%) for transmon A (B) using the analytical expressions from Ref. [S6]. The fraction of readout errors when the qubit is initialized in

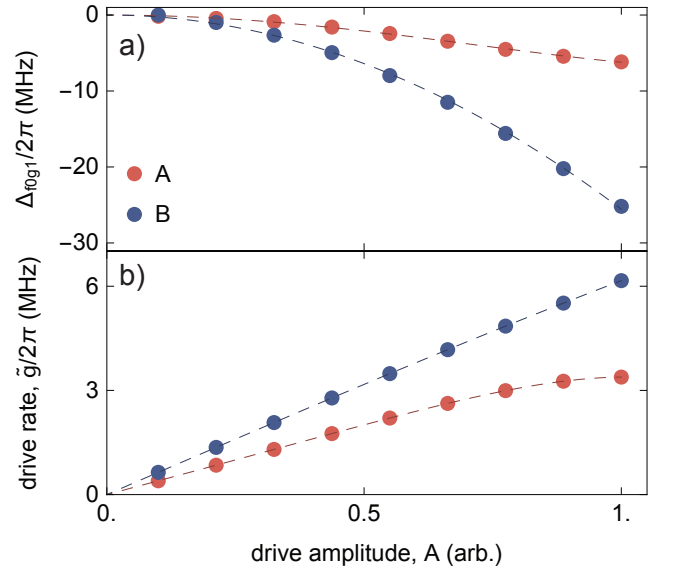


FIG. S3. a) ac Stark shift Δ_{f0g1} , and b) effective drive rate \bar{g} vs $|f0\rangle \leftrightarrow |g1\rangle$ drive amplitude A . The dashed line in a) and b) are polynomial fits to the data.

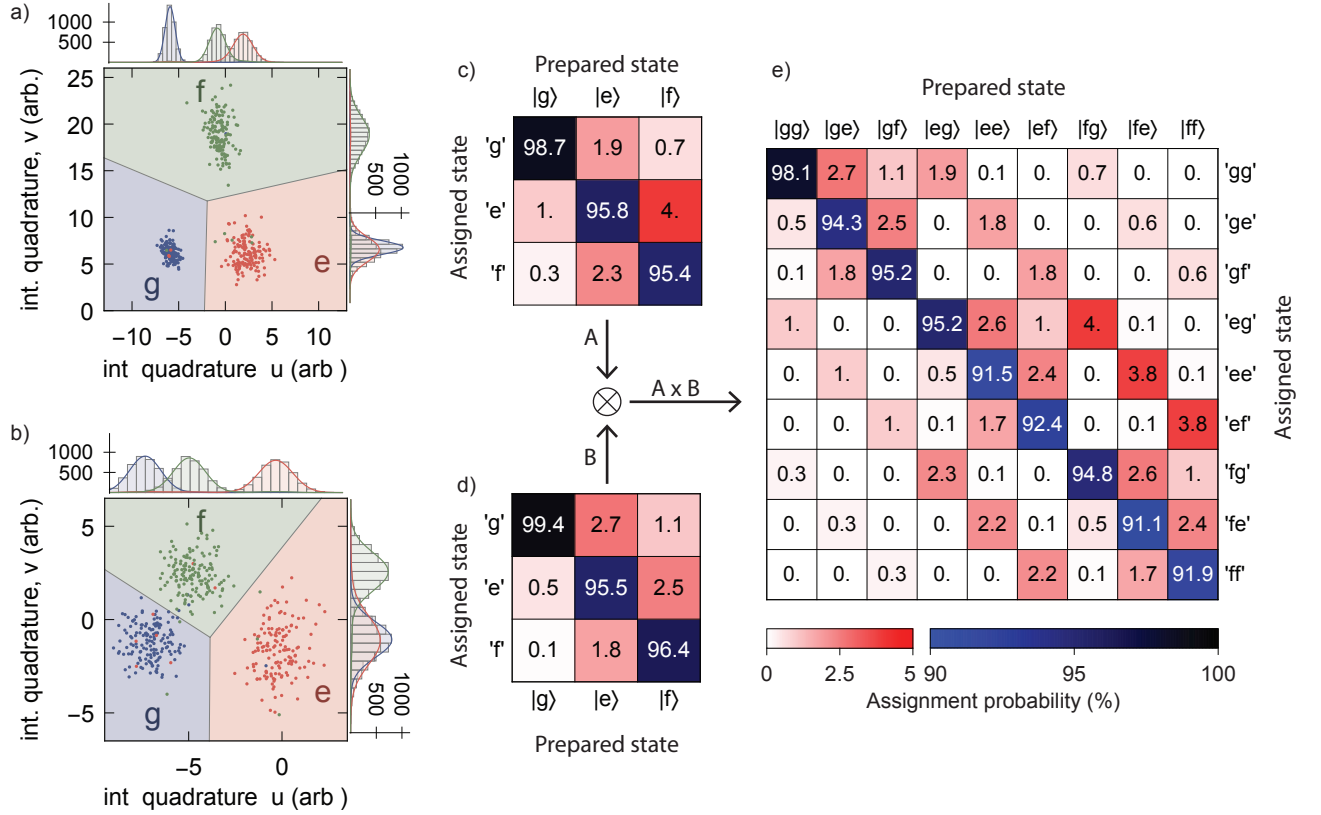


FIG. S5. a) and b) Scatter plot of the readout traces, integrated for 248 ns with optimal weights, with the qubit prepared in state $|g\rangle$ (blue dots), $|e\rangle$ (red dots) and $|f\rangle$ (green dots), for transmon A and B, respectively. The marginal histogram along the integration quadrature u and v is shown for each preparation state on the top and right axes, respectively. Solid-lines are density functions of the marginal three-modal, gaussian distribution estimated from the integrated traces, and scaled to fit the histograms. The $|g\rangle$, $|e\rangle$ and $|f\rangle$ assignment regions are shaded in blue, red and green, respectively. c) (resp. d)) Three-state assignment probability matrix extracted from the readout traces and the assignment region displayed in a) (resp. b)), for transmon A (resp. B). e) Two-qutrit assignment matrix calculated as the outer product of the single-qutrit assignment matrices.

increases (decreases) with exponential rate κ , limited by the coupling rate of the absorber (emitter) resonator to the waveguide. In this experiment, we minimize the protocol duration by choosing $\Gamma/2\pi = \min(\kappa_A, \kappa_B)/2\pi = 6.25$ MHz. The protocol duration could be further decreased by emitting photons with an asymmetric shape $\propto 1/(e^{\kappa_A t/2} + e^{-\kappa_B t/2})$. In this case both the falling and rising edge rates of the photon reach their upper limit, which is set by the external coupling rate of the transfer resonator of the emitter and absorber, respectively. However, such a scheme leads to only a minor reduction of the protocol duration while making the $|f0\rangle \leftrightarrow |g1\rangle$ pulse shape more complex. Therefore we selected a time-symmetric photon shape. We truncate the $|f0\rangle \leftrightarrow |g1\rangle$ pulse at $\pm 4.6/\Gamma$, where the drive amplitude is ramped down to 0 in 6 ns, to emit more than 98% of the photon in 246 ns.

For each node, we calibrate the relative time-of-arrival of drive and measurement pulses at the input port of the cryostat, using an oscilloscope. Then, to calibrate the relative timing between pulses at node A and pulses

at node B, we perform excitation transfer experiments sweeping the time between the application of the emission and absorption pulses. We select the time which maximizes the population transfer to transmon B. By comparing the envelopes of photons emitted from node A or B with this timing setting, we infer that the time between the application of the emission and absorption pulses corresponds to the photon propagation time plus a 10 ns lag (see Sec. S6). This optimal lag is due to the finite truncation of the $|f0\rangle \leftrightarrow |g1\rangle$ pulses. Such a truncated pulse emits a photon whose field amplitude is zero before the pulse start but decays exponentially once the pulse is finished, as the population remaining in the emitting transfer resonator continues to decay into the waveguide. Therefore the envelope of the emitted photon is shifted in time compared to the ideal target shape and is better absorbed by a delayed absorption pulse. Simulations of the experiment suggest that the excitation transfer is optimized with a 10 ns lag, in very good agreement with our observations. Accounting for the 28 ns photon propagation delay in the waveguide (as



FIG. S6. Photograph of the experimental setup during operation. The dilution refrigerator units, whose vacuum cans appear as white vertical cylinders, are connected to each other by the cryogenic link (long horizontal aluminum cylinder). The superconducting qubits and the cold waveguide are housed inside the dilution refrigerator units and the cryogenic link, respectively. The electronic instruments are stored in two black racks seen on the far sides of the picture.

estimated from lengths and group velocities of each section of the waveguide), we deduce that the absorption pulse is applied 38 ns after the emission pulse.

S4. QUTRIT READOUT

To measure transmon A (B), we apply a 4.692 GHz (4.680 GHz), gated microwave tone to the input port of the readout Purcell filter. Due to the qubit state dependent dispersive shift $\chi_r/2\pi = -4.1$ MHz (-7.9 MHz) of the readout resonator, the complex amplitude of the transmitted signal carries information about the transmon state, which results in a quantum non-demolition measurement of the transmon [S3].

For qutrit state detection, we amplify the signal using a near quantum-limited reflective JPA with 23.6 dB gain (21.3 dB) and 14 MHz bandwidth (47 MHz), pumped at 4.689 GHz (4.668 GHz). We cancel the JPA pump interferometrically at base temperature to avoid pump-induced qubit dephasing and saturation of subsequent amplifiers. We further amplify the signal at the 4K plate with high-electron-mobility transistors (HEMT), then at room temperature with (ultra-)low-noise amplifiers. The signal is then down-converted to 250 MHz, digitized at 1 Gs/s, and digitally down-converted to complex DC values by an FPGA using custom firmware (Fig. S4).

Over an acquisition window of duration $\tau = 248$ ns, the FPGA integrates the signal with two sets of weights to reduce the signal to two real-valued components u and v . The integration weights are chosen to maximize con-

trast in the $\{u, v\}$ plane between measurement traces obtained with the qubit initialized in either one of the states $|g\rangle$, $|e\rangle$ or $|f\rangle$. The integrated traces follow a tri-modal gaussian distribution, the parameters of which we estimate with a maximum likelihood approach. Each gaussian mode corresponds to the probability distribution of a measurement trace in the $\{u, v\}$ plane conditioned on the qubit being in a given state during the measurement. The FPGA then assigns the measurement trace to that state with mode center closest in the $\{u, v\}$ plane (see assignment regions in Fig. S5 a and b).

To calibrate the integration weights and mode centers used in the FPGA-based state assignment process, we prepare the transmon in $|g\rangle$, $|e\rangle$ or $|f\rangle$, record 4000 single-shot traces per prepared state, and run the analysis described above on this data set. We determine the single-shot readout assignment probability matrix R_A of transmon A (B), shown in Fig. S5 c (d), from the fraction of traces assigned to state ' j ' when the qubit was prepared in $|i\rangle$. We determine an average readout error probability of 3.4% (2.9%) from R_A (R_B), and of 6.2% from the joint system assignment probability matrix $R_A \otimes R_B$ (Fig. S5 e).

We determine the two-transmon state populations at the end of a given pulse sequence from the fraction of single-shot traces assigned to each state. We adjust this population estimate considering the readout errors by multiplying the population vector with the inverse of the two-transmon readout matrix. Because phase drifts of readout instruments lead to an increase in readout assignment error probability, each experiment contains measurements of reference states to estimate the assignment

probability matrix at the time of the experiment. We observe an increase of average readout errors to $\sim 5\%$ and $\sim 10\%$ for single and two qutrit readout, respectively.

S5. PHOTOGRAPH OF THE CRYOGENIC SYSTEM

A photograph of the cryogenic system used in this experiment is shown in Fig. S6.

S6. PHOTON ENVELOPE MEASUREMENTS

To assess the quality of the photon emission and absorption processes, we measure the mean photon field in the photon detection chain after emitting a photon from A, emitting a photon from B, or emitting a photon from A which we absorb at B, as illustrated by the pictograms in Fig. S7. In each case, we prepare the emitter qubit in $(|g\rangle + |f\rangle)/\sqrt{2}$ and apply an $|f0\rangle \leftrightarrow |g1\rangle$ pulse to emit symmetric-shape photons of state $(|0\rangle + |1\rangle)/\sqrt{2}$, with a non-zero average electric field $\langle a_{\text{out}}\rangle(t)$ proportional to the photon envelope $\phi(t)$.

We observe that photons emitted from B have the expected shape and bandwidth, as shown by the close match between the data points and results from master equation simulations using only an offset in time as a

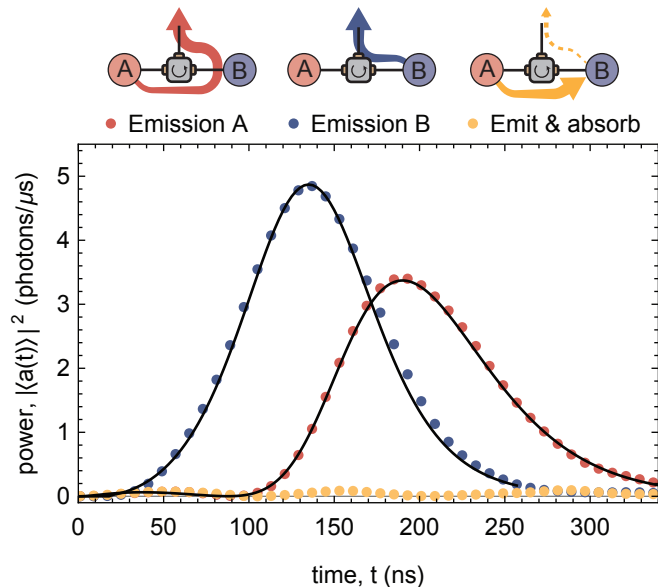


FIG. S7. Average electric field amplitude squared $|\langle a_{\text{out}}(t)\rangle|^2$ vs time of photons emitted from node B (blue), or emitted from node A and reflected from node B in presence (yellow) or absence (red) of an absorption pulse. The y -axis is normalized to obtain a unit integrated power for photons emitted from B. The solid lines are results of master equation simulations, with an offset in time to obtain the best agreement with the measurement.

fit parameter (solid line in Fig. S7). Photons emitted from A have a shape corresponding to the convolution of a hyperbolic secant shaped envelope with the time-response function of a reflection from resonator B. Here again, simulations agree well with the data.

As discussed in Sec. S3, the offsets in time fitted to the photon emitted from A and B differ by 10 ns. From this we infer that the emission pulse is applied $\Delta\tau_{AB} + 10$ ns before the absorption pulse, where $\Delta\tau_{AB}$ is the time it takes the photon to travel from node A to B.

Photons emitted from A have a 22.3% lower integrated power $\int |\langle a_{\text{out}}(t)\rangle|^2 dt$ compared to those emitted from B, which corresponds to the probability l_{AB} of losing a photon as it travels from A to B. We use this measured value of l_{AB} in master equation simulations of the experiment.

From the integrated power ratio of the photon field emitted from node A and reflected from node B in presence (yellow), or absence (red) of an absorption pulse at node B, we measure that 95.8% of the incoming photon is absorbed by node B.

S7. TOMOGRAPHIC RECONSTRUCTION

To perform quantum state tomography of a single qutrit, we measure the three-level population of the transmon with the single-shot readout method described in Sec. S4 after applying a tomography gate ${}^tR_n^\theta$ selected from the rotation set: $\mathcal{S} = \{\mathbb{1}, {}^{ge}R_x^{\pi/2}, {}^{ge}R_y^{\pi/2}, {}^{ge}R_x^\pi, {}^{ef}R_x^{\pi/2}, {}^{ef}R_y^{\pi/2}, ({}^{ef}R_x^{\pi/2} \cdot {}^{ge}R_x^\pi), ({}^{ef}R_y^{\pi/2} \cdot {}^{ge}R_x^\pi), ({}^{ef}R_x^{\pi/2} \cdot {}^{ge}R_x^\pi)\}$, where t denotes the qutrit transition, θ the rotation angle, and n the rotation axis. We reconstruct the three-level density matrix from this set of measured populations with a maximum likelihood method, assuming ideal tomography gates. This method extends to two-qutrit systems by applying all 81 pairs of local tomography gates from \mathcal{S} on the two transmons, and measuring their population in single-shot.

To characterize the transfer of qubit states from node A to node B, we prepare transmon A in one of the six mutually-unbiased qubit states $|g\rangle$, $|e\rangle$, $(|g\rangle + |e\rangle)/\sqrt{2}$, $(|g\rangle + i|e\rangle)/\sqrt{2}$, $(|g\rangle - |e\rangle)/\sqrt{2}$ or $(|g\rangle - i|e\rangle)/\sqrt{2}$ [S11], and transfer it to transmon B on which we perform full three-level quantum state tomography. We define the transfer process matrix χ as the representation of a completely positive trace-preserving map Λ which maps the input state ρ_{in} of qubit A to the output state ρ_{out} of qubit B through the relation $\rho_{\text{out}} = \Lambda(\rho_{\text{in}}) = \sum_{i,j} \chi_{ij} P_i \rho_{\text{in}} P_j$, where the operators P_i are in the set of modified Pauli matrices $\{\mathbb{1}, X = \hat{\sigma}_x, Y = i\hat{\sigma}_y, Z = \hat{\sigma}_z\}$ [S12]. Considering only the components of the output density matrices spanned by states $|g\rangle$ and $|e\rangle$, we obtain the two-level process matrix χ using a maximum likelihood method.

Due to leakage to the $|f\rangle$ level of the transmons during the entanglement protocol, the entangled state cannot be rigorously represented by a two-qubit density matrix. However, to be concise and give standard metrics of en-

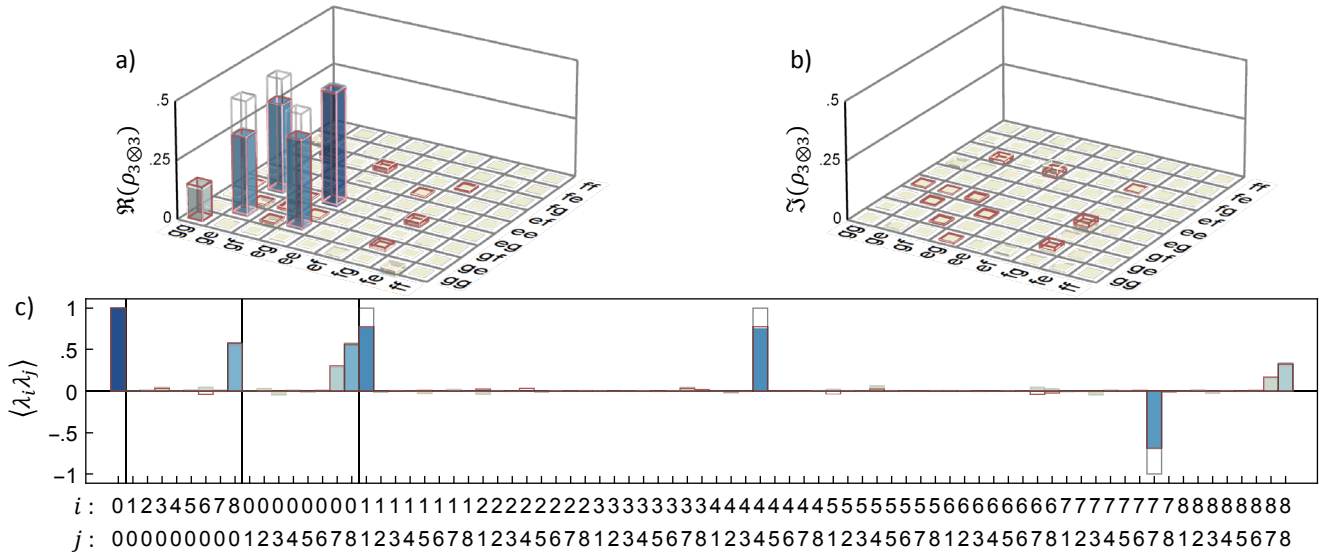


FIG. S8. a) Real, and b), imaginary part of the two-qutrit entangled state $\rho_{3 \otimes 3}$. c) Expectation value of the two-qutrit Gell-Mann operators of state $\rho_{3 \otimes 3}$. In all panels, blue solid bars, gray wireframes and red wireframes represent the reconstructed, ideal and simulated values, respectively.

tanglement, we reduce the reconstructed two-qutrit state $\rho_{3 \otimes 3}$ (Fig. S8) to a two-qubit state ρ consisting of the two-qubit elements of $\rho_{3 \otimes 3}$. This reduction method leads to states with non-unit trace, but it preserves the fidelity,

and gives a conservative estimate to the concurrence compared to a projection of $\rho_{3 \otimes 3}$ on the set of physical two-qubit density matrices.

-
- [S1] P. Kurpiers, T. Walter, P. Magnard, Y. Salathe, and A. Wallraff, *EPJ Quantum Technology* **4**, 8 (2017).
- [S2] D. M. Pozar, *Microwave Engineering*, 4th ed. (Wiley & Sons, Inc., New Jersey, USA, 2012).
- [S3] T. Walter, P. Kurpiers, S. Gasparinetti, P. Magnard, A. Potočnik, Y. Salathé, M. Pechal, M. Mondal, M. Oppliger, C. Eichler, and A. Wallraff, *Phys. Rev. Applied* **7**, 054020 (2017).
- [S4] K. Geerlings, Z. Leghtas, I. M. Pop, S. Shankar, L. Frunzio, R. J. Schoelkopf, M. Mirrahimi, and M. H. Devoret, *Phys. Rev. Lett.* **110**, 120501 (2013).
- [S5] K. Serniak, M. Hays, G. de Lange, S. Diamond, S. Shankar, L. D. Burkhardt, L. Frunzio, M. Houzet, and M. H. Devoret, *Phys. Rev. Lett.* **121**, 157701 (2018).
- [S6] P. Magnard, P. Kurpiers, B. Royer, T. Walter, J.-C. Besse, S. Gasparinetti, M. Pechal, J. Heinsoo, S. Storz, A. Blais, and A. Wallraff, *Phys. Rev. Lett.* **121**, 060502 (2018).
- [S7] F. Motzoi, J. M. Gambetta, P. Rebentrost, and F. K. Wilhelm, *Phys. Rev. Lett.* **103**, 110501 (2009).
- [S8] M. Pechal, L. Huthmacher, C. Eichler, S. Zeytinoglu, A. A. Abdumalikov Jr., S. Berger, A. Wallraff, and S. Filipp, *Phys. Rev. X* **4**, 041010 (2014).
- [S9] P. Kurpiers, P. Magnard, T. Walter, B. Royer, M. Pechal, J. Heinsoo, Y. Salathé, A. Akin, S. Storz, J.-C. Besse, S. Gasparinetti, A. Blais, and A. Wallraff, *Nature* **558**, 264 (2018).
- [S10] O. Morin, M. Körber, S. Langenfeld, and G. Rempe, *Phys. Rev. Lett.* **123**, 133602 (2019).
- [S11] S. J. van Enk, N. Lütkenhaus, and H. J. Kimble, *Phys. Rev. A* **75**, 052318 (2007).
- [S12] I. L. Chuang and M. A. Nielsen, *J. Mod. Opt.* **44**, 2455 (1997).